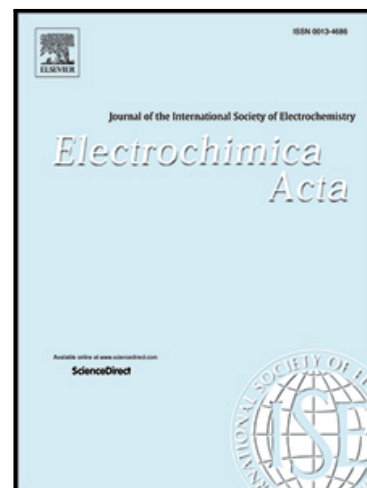# Journal Pre-proof

High Performance Sodium-ion Battery Anode using Biomass Derived Hard Carbon with Engineered Defective Sites

Thileep Kumar Kumaresan , Shanmugharaj Andikkadu Masilamani , Kalaivani Raman , Smagul Zh. Karazhanov , Raghu Subashchandrabose

Please cite this article as: Thileep Kumar Kumaresan , Shanmugharaj Andikkadu Masilamani , Kalaivani Raman , Smagul Zh. Karazhanov , Raghu Subashchandrabose , High Performance Sodium-ion Battery Anode using Biomass Derived Hard Carbon with Engineered Defective Sites, *Electrochimica Acta* (2020), doi: https://doi.org/10.1016/j.electacta.2020.137574

This is a PDF file of an article that has undergone enhancements after acceptance, such as the addition of a cover page and metadata, and formatting for readability, but it is not yet the definitive version of record. This version will undergo additional copyediting, typesetting and review before it is published in its final form, but we are providing this version to give early visibility of the article. Please note that, during the production process, errors may be discovered which could affect the content, and all legal disclaimers that apply to the journal pertain.

Highlights

- BFMI biomass derived defective hard carbon (HC) in mixed gas environment is

  reported

- Controlled CO_2 purging in N_2 environment at $1400^{o}C$ leads to HC with defective sites

- Prepared HC anode (BFHC-NC$_5$) display discharge/charge capacities of 413/358

  mAh g^{-1}

- Defective HC anode renders outstanding capacity retention of 86.6 % at first cycle.

- Prepared hard carbon records outstanding rate-performance in sodium-ion storage for

  500 cycles.

High Performance Sodium-ion Battery Anode using Biomass Derived Hard Carbon with Engineered Defective Sites

Thileep Kumar Kumaresan[a], Shanmugharaj Andikkadu Masilamani[b], Kalaivani Raman[a],

Smagul Zh. Karazhanov[c], Raghu Subashchandrabose[b*]

[a]Department of Chemistry, Vels Institute of Science, Technology & Advanced Studies (VISTAS), Chennai- 600 117, Tamilnadu, India.

[b]Centre for Advanced Research & Development (CARD) / Chemistry, Vels Institute of Science, Technology & Advanced Studies (VISTAS), Chennai- 600 117, Tamilnadu, India.

[c]Department for Solar Energy, Institute for Energy Technology (IFE), Kjeller 2027, Norway.

*Corresponding author: Phone: +91 9790995822. E-mail: subraghu_0612@yahoo.co.in

Abstract

Defective hard carbons are deliberated as promising candidates for sodium-ion battery (SIB) anodes of this decade. Recently, several groups have discussed the structure-property correlation which correlates the slope capacity in charge/discharge profile curves to the binding of sodium-ions on the structural defective sites of the hard carbon. In order to validate these correlations, herein we report for first time the preparation of defective hard carbon materials from Borassus flabellifer male inflorescence *via* controlled thermal activation process using Nitrogen (N_2) and Carbon dioxide (CO_2) gas mixtures and its subsequent usage as anode material in sodium-ion battery. When used as sodium-ion battery anode, the prepared hard carbon displayed outstanding reversible discharge/charge capacities of 413/358 mAh g^{-1} and superior initial capacity retention of 86.6 %, which is the highest ever reported value to date alongwith a overwhelming cycling stability. The notable

improvements can be correlated to the broken edges present in the hard carbon surface as well as the randomly distributed micro-nano structured pores in the system as revealed by the morphological characterizations. Thus, the reported research work paves way in developing novel low cost and high performance micro-nano structured defective hard carbon anode materials for Sodium-ion batteries.

Keywords: Defective hard carbons, Sodium-ion batteries, Borassus flabellifer, Sodiation mechanism.

1. Introduction

Sodium-ion batteries (SIBs) are ascribed to be the most proficient substitutes to lithium based rocking chair batteries (LIBs) for the present-day energy storage applications due to their natural abundance as well as the lower cost of sodium stockpiles.[1, 2] However, for designing commercially feasible, safer and long life SIBs there is a need for the discovery of novel electrode and electrolyte systems.[3] Owing to its low cost and simple processing requirements, carbonaceous material like graphite is widely employed as anode for lithium or sodium based rocking chair batteries. Anyhow, fabrication of the sodium-ion based rocking chair batteries (SIBs) is a difficult task, since the ionic radii of the sodium-ion (0.106 nm) is about 55% higher in comparison to the ionic radii of lithium-ion (0.076 nm).[4-6] Also, the thermodynamic instability of sodium-ion based graphite intercalation compounds (GIC) restrict its potential application aspect in the fabrication of SIBs.[7] To overcome this issue, various carbon nanostructures with one dimension (carbon fibres, nanotubes), two dimension (heteroatom doped-graphene) and three dimension (porous carbon structures) have been extensively applied as potential anode materials for SIBs.[8-10] Alternatively, numerous attempts have also been made in designing novel electrode materials viz., Metal,[11-13] organic compounds,[14] metal oxides, sulfides and alloys etc.[15-18]

In contrast to the various nanostructured carbon based anodes, hard carbon materials (HCM) derived from waste resources such as biomass has received extensive attention worldwide, thanks to the scalable synthetic procedures, lower operating voltages and superior reversible capacities. [19] The regular packed structure of HCM's consisting of nano-crystalline domains of few layered graphene sheets, is generally represented as the "Falling card model". Widespread research has been done by various research groups on the preparation and characterization of hard carbon materials derived from various biomass waste resources such as fruit peels, shells, husks, grasses and leaves.[20-31] However, owing to the parasitic chemistry involved in the electrolyte degradation on the HCM anodes on the first electrochemical sodium-ion intercalation/de-intercalation higher irreversible capacity is displayed and upon cycling at low current densities unacceptable Coulombic efficiencies were observed.[32, 33] Mostly in the field of batteries, biomass-derived carbon materials are assembled as graphene surfaces with significant defects that can generally be categorized as turbostratic carbon / hard carbon. Moreover, various studies recorded the incorporation of biomass-derived carbons in batteries.[34-37] In fact, defective structures alike these have a greater slope capacity when compared to the conventional hard carbon. The sodium-ion storage mechanism for hard carbon has recently been updated, where sodium-ion binding to structural defects is due to the increased potential slope efficiency in galvanostatic Charge/discharge (GCDs) profiles.[38, 39] Furthermore, the recent report made by Ji et al. on low temperature microwave synthesized defective hard carbon also corroborates the above fact.[40] The electrochemical features of electrode materials derived from biomasses extremely depend on the natural properties of the biomass and the preparation method of the carbon materials from the biomass. Synthetic processes of hard carbon materials are environmental friendly, low cost, and with green synthesis methods. To ensure efficient

sodium-ion intercalation in the hard carbon structures the pyrolysis procedure is conducted under high temperatures (1000-1800°C) and inert atmosphere [41].

The male inflorescences obtained from Borassus flabellifer, a tall palm is one among the most abundant biomass material originating from the warm tropical portions of India and worldwide [42, 43]. Owing to the presence of various polyaromatic groups, this biomass could render a classic hard carbon, when processed under stipulated experimental conditions. However, interestingly, to the best of our knowledge, no research has been done using this biomass material. In the present study, defective hard carbon was prepared from Borassus flabellifer male inflorescence under controlled thermal (1400°C) activation process using Nitrogen (N_2) and carbon dioxide (CO_2) gas mixtures. We prepared three types of hard carbon products by simply varying the gas flow rate of N_2 and N_2-CO_2 mixtures in ratio of 100, 100:5 and 100:10 ml respectively. The obtained products (gas flow 100 ml/min, 100:5 ml min^{-1} and 100:10 ml min^{-1} referred as BFHC-NC_0, BFHC-NC_5, BFHC-NC_{10} respectively) lead to hard carbon materials with unexpectedly highly defective nature and higher sodium-ion storage capacity. Galvanostatic charge/discharge, cyclic voltammetry, impedance spectroscopy were performed to understand the sodium-ion storage capacity contribution from each material and their capacities resulting from the diffusion controlled process. For the first time, defective hard carbon (N_2:CO_2; 100:5 ml min^{-1} gas flow ratio with 1400°C) with extreme rough surface, wrinkles, enhanced broken edges, and randomly distributed pore walls have been developed from Borassus flabellifer male inflorescences. These outstanding structural features of the prepared hard carbon benefits the formation of stable SEI film and efficient access to the electrolyte ions, with boosted ion diffusion and electrochemical property for SIBs.

2. EXPERIMENTAL SECTION

2.1 Materials

The carbon precursor, Borassus flabellifer male inflorescences (BFMI) were obtained from Mukkur village, Thiruvannamalai district, Tamilnadu, India. Analytical standard hydrochloric acid (HCl), was purchased from Recon in Chennai. The solvents were used without further purification. The reagents used are of high purity degree, and were supplied by different suppliers; Carbon Black Super P (TOB, china), Carboxymethyl cellulose (CMC), Poly (acrylic acid) (PAA), Sodium perchlorate (99.9%), Ethylene Carbonate (EC) and Diethyl Carbonate (DEC) battery grade (Sigma-Aldrich).

2.2 Synthesis of Defective Hard Carbon material (HCM) from Biomass

Borassus flabellifer male inflorescences (BFMI) were collected, cleansed using de-ionized water for repeatedly, and dried thoroughly in sunlight for 12 hrs. In the typical HCM's synthetic procedure, 20 g of the carbon precursor was initially pre-carbonized at $300^{o}C$ for 2 hrs. Subsequently, pre-carbonized powder was pyrolyzed under the mixed gas environment (nitrogen and carbon di-oxide (NC)) in a horizontal cylindrical furnace by following steps as indicated (shown in **Figure S1**). Initially, quartz crucible loaded with 8.5 g of pre-carbonized powder was kept in the tubular furnace and purged with nitrogen (N_2) gas for 30 minutes (100ml/min), and then the temperature was gradually elevated to the specified activation temperature ($1400^{o}C$) at a heating rate of 5 °C/min. Once the furnace temperature reached the desired value, carbon-di-oxide (CO_2) was purged along with the N_2 purging (100 ml/min) for 2 hrs. The final product of the defective hard carbon materials (BFHC-NC_x) were then powdered washed with dilutes 1M HCl for about 12 hrs. and finally washed with deionized water to remove impurities. The synthesized samples were designated as BFHC-NC_x, where x indicates the CO_2 gas flow rate used in the preparation of hard carbon (x= 0, 5, 10). Thus, the prepared hard carbon materials (BFHC-NC_x) were designated as BFHC-NC_0, BFHC-NC_5 and BFHC-NC_{10} respectively.

2.3 Preparation of the working electrodes:

Coin cells (CR2032) were used to conduct the electrochemical experiments. The working electrodes of biomass derived nano structured hard carbon were fabricated by coating the slurry containing 85 wt% active material, 10 wt% activated carbon and by 5 wt% of binders (2.5% CMC and 2.5% PAA) on an Aluminium foil. The half-cells were constructed under argon atmosphere in a glove box (Etelux-Lap 2000, china) where oxygen and water levels were <1 ppm in a 2-electrode system with pure sodium metal as the counter and reference electrodes of the coin cells (CR2032). 1 M $NaClO_4$ in a mixture of EC and DEC (3:7 v/v) was used as the electrolyte. The galvanostatic charge/discharge (GCD) was examined in the Neware battery tester (5V, 10mA, china). The cyclic voltammetry (CV) performance of the half-cell SIBs were studied by biologic electrochemical workstation (Biologic, France).

2.4 Physical Characterizations:

The morphology of the synthesized micro-nano organized highly defective hard carbons were studied via Quattro S scanning electron microscope. Raman analysis of the defective hard carbons were recorded in Alpha 300 R, WI Tec GmbH at room temperature using 532 nm laser excitation. TEM micrographs were obtained by using the FEI-Tecnai G2 20 Twin transmission electron microscopy (TEM).BETSORP max, Microtrac BEL, was used to surface areas of the prepared defective hard carbon materials from the N_2 adsorption–desorption isotherm measurements at 77 K following the Brunauer–Emmett–Teller (BET) method. The pore size distribution (PSD) of the materials were calculated using the non-linear density functional theory (NLDFT) model. X-ray photoelectron spectroscopy (XPS) was acquired on a Nexsa Surface Analysis System from Thermo Fisher Scientific using 300 μm Al Kα X-ray source. X-ray diffraction (XRD) patterns was performed using a Rigaku Smart Lab with the Cu Kα radiation, set at the operating voltage of 40 kV (λ = 0.154 nm) to study the crystallinity of the structures.

XRD characteristics were evaluated according to the formula [44]

The layer stacking distance (L_c) and the longitudinal size of structural elements (L_a) were calculated according to the formula (Scherrer equation)

$$L_c \& L_a = \frac{K\lambda}{\beta \cos\theta} \qquad (1)$$

Where, K is scherrer constant (K=0.9 for L_c & K=1.84 for L_a), λ is the radiation wavelength, β is the half-height width of the (002) reflection, θ is the reflection angle of (002) or (100),

The layer packing density (ρ) was evaluated from the given formula

$$\rho = \frac{0.762}{d_{002}} \qquad (2)$$

The number of layers in a stack was calculated using given formula

$$n = \frac{L_c}{d_{002}} + 1 \qquad (3)$$

3. Results and Discussions

3.1 Morphology and structure of prepared hard carbon (BFHC)

The schematic representation of Borassus flabellifer male inflorescences (BFMI) derived hard carbon material (BFHC-NC$_x$) is shown in **Figure 1**. As shown in the figure, BFMI consisting of spirostane-type steroid saponins (*viz.*, borossosides and dioscin), steroidal glycosides and carbohydrates (*viz.*, glucose) [45,46] is expected to form turbostatic hard carbon materials with varying degrees of disordered to ordered carbon content depending on the gas flow rate at higher temperature (1400°C). **Figure 2** is the TEM result of the defective hard carbon displaying higher degree of the disorderness, corroborating the presence of certain degree of the amorphous carbon clusters in the prepared BFHC-NC$_0$ as depicted in **Figure 1**. Upon the introducton of the controlled CO_2 gas flow alongwith N_2 (BFHC-NC$_5$) flow at the pyrolysis temperature 1400°C, notable rise in the defective graphitic microcrystals in the pool of disordered carbon is observed resembling its turbostatic nature. Randomly distributed amorphous carbon clusters are completely degraded at lower CO_2 gas flow rate resulting in the higher degree of defective graphitic microcrystals in the prepared hard carbon

(BFHC-NC$_5$). High resolution TEM images showed the presence of disordered carbon in BFHC-NC$_5$. Further increment in CO$_2$ gas flow rate resulted in the loss of graphite microcrystals leading to the defective sites, thereby formation of higher degree of disordered carbon (BFHC-NC$_{10}$). In addition, notable rise in nanopores encircled by turbostratic nanocrystallites is observed in hard carbons prepared in mixed gas environment (BFHC-NC$_5$ & BFHC-NC$_{10}$) in comparision to the hard carbons prepared under nitrogen environment (BFHC-NC$_0$). Presence of disordered and graphitic carbon phase in a representative hard carbon material (BFHC-NC$_5$) is clearly visualized in the atomic force microscopy results (**Figure 2(e,f)**). Included in Figure are the amplitude (e) and phase (f) images of the BFHC-NC$_5$ sample, which depicts the existence of disordered carbon phase with randomly distributed spherical carbon clusters (blue circle), ordered carbon phase consisting array of carbon platelets (red circle) and stacked carbon layers with broken edges (green circles).

To further validate the structural variation upon thermal gas activation, diffraction studies were done for the HCMs and are included in **Figure 3(a) & S2**. All the prepared hard carbon materials (BFHC-NC$_x$) exhibited two broad XRD diffraction patterns at 2θ values of ~25° (002) and at ~43° (100), corroborating the existence of randomly distributed microcrystalline graphitic planes in the pool of disordered carbons as depicted in **Figure 1** (Schematic diagram), implying the turbostratic nature of the prepared BFHC-NC$_x$ (**Figure 3(a)**) [47]. Depending on the mixture of gas flow rate (NC$_x$; x = 0, 5, 10), though there is no noticeable variation in 2θ values of (002) diffraction peak, relative decrement in the overall full width at half height maximum (FWHM) is observed (**Table 1**). For instance, overall FWHM values of (002) diffraction peak of HCM prepared at various gas flow are noted to be 8.15^o (BFHC-NC$_0$), 5.84^o (BFHC-NC$_5$) and 7.37^o (BFHC-NC$_{10}$) respectively revealing the enhanced degree of graphitic crystals with increasing gas flow rate at higher temperature (**Figure 3 (a)&S2**). To get more insights in the turbostratic nature of the prepared BFHC-NC$_x$,

X-ray diffraction patterns were analysed by profile fitting approach reported by Cao et al., [48] to distinguish different regions of the broad (002) diffraction and the results are included in **Figure S2(a-c)**. The prepared BFHC-NCx samples display two broad peaks, which are correlated to the (002) diffraction patterns of disordered and graphitic carbon structures [48]. The phase fraction of disordered and graphitic carbon is calculated by determining the area under the profile fitted peaks and the results are tabulated in **Table 1**. The ratio of disordered to graphitic phase (P_D/P_G) are observed to be 0.93 (BFHC-NC$_5$) and 1.07 (BFHC-NC$_{10}$) revealing the enhancement in the graphitic crystalline phases on using mixed gas environment (N_2/CO_2), when compared to the hard carbon (BFHC-NC$_0$, P_D/P_G, 1.29) prepared under simple nitrogen environment. To get more insights in the turbostratic nature of the prepared BFHC- NC$_x$, de-convolution of (002) diffraction peak has been done and the results are as shown in **Figure S2(a-c).** [47] All the prepared BFHC- NCx display two broad peaks, which can be correlated to the (002) diffraction patterns of disordered and ordered carbon structures.[48] The relative content of the disordered and ordered phases, calculated from the peak intensities of the respective components, showed a systematic variation with increasing CO_2 gas flow rate. For instance, progressive decrement in disordered phase with simultaneous increment in ordered phase content is noted on increasing the CO_2 gas flow rate at 1400°C (**Table 1**). The average d-spacing values of disordered and ordered carbon structures were calculated using corresponding 2θ values and the results are shown in **Table 1**. The d-spacing values of disordered carbon are noted to be 3.70 Å (BFHC-NC$_0$), 3.85 Å (BFHC-NC$_5$) and 3.82 Å (BFHC-NC$_{10}$) respectively. Similarly, d-spacing values of graphitic carbon structures are observed to be 3.20 Å (BFHC-NC$_0$), 3.37 Å (BFHC-NC$_{10}$) and 3.40 Å (BFHC-NC$_5$) respectively. Similar trend is noted on the average crystallite size (L_C), layer packing density (ρ) and number of stacked layers (n), calculated for both disordered and ordered carbon structures (**Table 1**). Also, systematic increment in the average layer

dimension (L_a), calculated from (100) graphitic crystal plane using Scherer equation, is observed revealing the lateral growth of graphitic microcrystals with increasing CO_2 gas flow rate at 1400°C (Table 1). At only the nitrogen gas flow at 1400°C, pre-carbonized soft carbons (~300°C) derived from saponins, glycosides and carbohydrates exists in the intermediate steps, where the pool of the disordered hard carbons with least degree of graphitic phases is slowly being converted into microcrystalline graphitic crystals with the variation in their dimensional orders as shown in the schematic representation (**Figure 1**). Varying the gas flow with thermal treatment at 1400°C have much influence on the degree of structural growth of the perfect graphitic crystals, rather significant variation in turbostratic graphitic structures with broken crystal edges as depicted in the TEM results (**Figure 2).** This fact is well corroborated from the systematic rise in both crystallite size (L_C) and layer dimension (L_a) values of microcrystalline graphitic planes with optimum gas flow (100:5) (Table 1). Among the experimental results, shows the increasing the CO_2 gas flow from 5ml min^{-1} to 10ml min^{-1} high loss of carbon yield and decrease the surface area these might be decreasing the crystallite size (L_C) and layer dimension (L_a).

The existence of the turbostratic nature of the microcrystalline graphitic planes in the prepared biomass derived hard carbon materials is further revealed from the Raman spectroscopic results (**Figure 3(b)&S3**). Irrespective of the CO_2 gas flow rate, Raman spectra of all the hard carbons showed two prominent peaks at ~1350 cm^{-1} (D band) and at ~1600 cm^{-1} (G band), which are correlated to the defective or disordered graphitic sp^2 structures (A1g phonon mode vibrations) and ordered or perfect graphitic sp^2 crystalline features (E$_{2g}$ phonon mode vibrations) of the prepared hard carbon materials. To get additional informations on the structural features of the prepared hard carbon materials (BFHC-NC$_x$), de-convolution of Raman results was also done and the results are enclosed in **Figure S3**. De-convolution of Raman results displayed five intense peaks in all the prepared hard carbon

materials, implying the contributions induced by transverse optical (TO) mode vibrations of isolated pentagonal structures with eclipsed configurations (D_3 peak, ~1100 cm^{-1}) along with the broad peaks (G_2 and D_2) corresponding to the amorphous sp^2 carbon clusters with bond disorder, whereas the sharp peaks (G1 and D1) is corroborated to the winding short basal plane of graphite with bond angle order (**Figure S3(a-c)**).[49, 50] From the de-convoluted Raman spectra, noticeable variations in peak position, FWHM and peak intensities are observed for the prepared BFHC-NCx on varying the CO_2 gas flow rate. The prepared BFHC-NCx display slight variation in G_1 peak ranging from 1580~1600 cm^{-1} (BFHC-NC$_0$, 1602 cm^{-1}; BFHC-NC$_5$, 1580 cm^{-1}; BFHC-NC$_{10}$, 1590 cm^{-1}) revealing the formation of nanocrystalline graphitic planes consistent of the three stage model diamond amorphization from graphene.[51] Alternatively, FWHM of the D_1 peak, a parameter used to interpret structural defects in the graphitic phases, decreases corroborating the noticeable decrement in the basal plane defects with optimum CO_2 gas flow conditions (BFHC-NC$_0$, 117 cm^{-1}; BFHC-NC$_5$, 64 cm^{-1}; BFHC-NC$_{10}$, 76 cm^{-1}). On the contrary, varying the gas flow rate at 1400°C, results in the variation of G_2 peak position (BFHC-NC$_0$, 1546 cm^{-1}; BFHC-NC$_5$, 1489 cm^{-1}; BFHC-NC$_{10}$, 1506 cm^{-1};) along with the noticeable increment in FWHM (BFHC-NC$_0$, 161 cm^{-1}; BFHC-NC$_5$, 220 cm^{-1}; BFHC-NC$_{10}$, 199 cm^{-1}) of G_2 peak, a measure of bond angle distortion induced structural disorders, brought about the rise of structural defects in the disordered carbon phase of the prepared BFHC-NCx. Significant reduction in I_{D1}/I_{G1} (BFHC-NC$_0$, 1.35; BFHC-NC$_5$, 0.77, BFHC-NC$_{10}$, 1.03) and rise in I_{D2}/I_{G2} (BFHC-NC$_0$, 0.36; BFHC-NC$_5$, 0.86; BFHC-NC$_{10}$, 0.80) revealed the growth of both graphitic basal planes and disordered carbon clusters, thus promoting the growth of overall grain size of turbostratic carbons and disorders, with CO_2 gas flow rate at 1400°C [52] Further analysis on the second order transitions of the Raman peaks in the spectral range of 2500~3000 cm^{-1} displayed two prominent peaks corresponding to 2D (~2635 cm^{-1}) and D+D′ (~2925 cm^{-1}) bands for all the

prepared BFHC-NCx. Since, the prepared BFHC-NC$_x$ are turbostratic in nature, single Lorentzian fit has been made for the 2D and D+D′ peaks to determine the FWHM values.[53] As expected FWHM values are broader for all the BFHC-NC$_x$ with systematic varying on the CO$_2$ gas flow rate. The FWHM values are noted to be 358 (BFHC-NC$_0$), 280 (BFHC-NC$_{10}$) and 261 cm^{-1} (BFHC-NC$_5$), respectively with drastic decrease in D+D′ peak intensities (**Figure S3(d-f)**). Relative decrement in FWHM and intensity values of 2D and D+D′ peaks further supports the structural growth of the graphitic planes on varying the CO$_2$ gas flow rate. In consistent with the XRD results, Raman spectroscopic studies of the prepared BFHC-NC$_x$ revealed the formation of ordered graphitic planes constituted of imperfect polycyclic hydrocarbons in the pool of amorphous carbon clusters derived from the pyrolyzed product of non-aromatic side chains. To reveal the bonding configuration and chemical composition of the prepared BFHCM's-NC$_x$, X-ray photoelectron spectroscopic (XPS) characterization was done and the results are included in **Figure S4 and Table S1.**

The pore size distribution and the nitrogen adsorption–desorption isotherms of the prepared Borassus flabellifer male inflorescences derived hard carbon material (BFHC-NC$_x$) are as displayed in **Figure 3(c-f)**. In consistent to the IUPAC classification, all the prepared BFHC-NC$_x$ samples show a typical type-II isotherm, specifying the micro-nanostructured features of the materials. Appearance of the hysteresis loop in all the prepared BFHC-NC$_x$ samples showed a typical H$_3$-type verifying the existence of non-rigid plates like aggregates which gave rise to the slit-shaped pores on the material surface (**Figure 3(a-c)**). The parameters such as BET surface area, volume of adsorbed nitrogen on the carbon surface (V$_m$), total pore volume (V$_P$) and mean pore diameter (D$_P$) were found by BET isotherms and the outcomes are comprised in **Table 2**. Surface area was decidedly greater for BFHC-NC$_x$ prepared nitrogen: carbon-di-oxide flow rate (NC$_5$) at 1400°C (BFHC-NC$_5$; 18.87 m^2 g^{-1}) confirming its high porosity when compared to the hard carbon materials (BFHC-NC$_x$)

prepared at only nitrogen gas flow *viz*., (BFHC-NC$_0$; 4.08 m^2 g^{-1}) and nitrogen: carbon-di-oxide flow rate (NC$_{10}$) at 1400°C (BFHC-NC$_{10}$; 8.86 m^2 g^{-1}). Significantly, higher surface area achieved for the defective hard carbon of BFHC-NC$_5$ ensures the fast sodium-ion storage and is beneficial over volume change taking place on sodium-ion insertion-extraction development. Included in **Figure 3(d)**, the pore size distribution curves of the prepared hard carbon materials (BFHC-NC$_x$). From the PSD curves, it is quite evident that all the prepared BFHC-NC$_x$ display intense pore volume peaks at varying pore sizes *viz.*, < 2 nm and between 2~5 nm. The pore volume values at lower pore sizes (< 2 nm) are observed to be 0.025 (BFHC-NC$_0$), 0.05 (BFHC-NC$_5$) and 0.04 cm^3 g^{-1} (BFHC-NC$_{10}$), respectively. Similarly, the pore volume values in the pore size range of 2~5 nm are noted to be 0.00534 (BFHC-NC$_0$), 0.00945 (BFHC-NC$_5$) and 0.000752 cm^3 g^{-1} (BFHC-NC$_{10}$). The systematic increment in pore volume peak intensities at lower pore size (<2 nm) with notable decrement in the pore size range of ~2-5 nm on increasing gas flow rate, is attributed to the growth of carbon nanostructures along with the presence of microporous/mesoporous carbon structures in the prepared carbon from biomass [54]. The rough surface with wrinkles, enhanced broken edges and randomly distributed pore walls structure of prepared hard carbon (BFHC-NC$_x$) benefits to form a stable SEI film and efficient access of electrolyte ions to the carbon surface with boosted ion diffusion and electrochemical property for SIBs.

3.2 Electrochemical performances of the hard carbon materials

3.2.1 Open Circuit Voltage and Na-ion diffusion properties of defective hard carbon

The open circuit voltages (OCV) a measure of sodium-ion storage in the carbon surface at zero potential, increases revealing the enhancement in the sodium-ion diffusion property on varying the CO$_2$ gas flow rate (0~10 ml min^{-1}).

Na-ion diffusion properties can be correlated to the open circuit voltages (OCV) with varying Na coverage on defective hard carbon using the relation.

$$OCV = (EHC+xENa-EHCNax)/x \qquad (4)$$

Where xENa, EHC Nax and EHC represent the energy storage capacity delivered by bulk sodium metal (x corresponds to number of Na-ions), total energy released with and without multi Na-ion adsorption on the defective hard carbon materials (Er et al., ACS Appl. Mater. Interfaces, 2014; Aydinol et al., J. Power Sources, 1997). [55,56]From the above equation, one can clearly visualize the relation between the OCV and Na-ion energy storage capacity. Higher OCV indicates the available sites for Na-ion adsorption on defective hard carbon, which promotes the Na-ion diffusion from the bulk sodium metal (anode) to defective hard carbon sites (cathode).

In addition, the maximum capacity (CM) delivered by defective hard carbon can be correlated by the following equation

$$CM = cxF/MHC \qquad (5)$$

Where c is the number of adsorbed Na-ion, x represents the number of electrons involved in the electrochemical process, F is the Faraday constant (26801 mAh mol^{-1}) and MHC is the molecular weight of the defective hard carbon. From the above relation, we can clearly corroborate the role of electrons involved in the electrochemical process on the overall capacity.

3.2.2 Cyclic Voltammetry studies

To substantiate the role of the structure on the energy storage properties, biomass derived defective hard carbon prepared at various conditions (BFHC-NC$_0$; BFHC-NC$_5$; BFHC-NC$_{10}$) have been evaluated as SIB anodes in half-cell configuration using the Na-metal as the counter and reference electrode and sodium perchlorate (1 M NaClO$_4$ in EC: DEC (3:7)) based electrolyte.

Shown in **Figure 4(a-c)** are the cyclic voltammograms (CV) (first, second and fifth cycles), measured at a potential range of 0.001~2.5 V at the scanning speed of 5 mV s^{-1} of the

BFHC-NC$_x$ based SIBs. Insertion and extraction of the sodium-ion in all the prepared BFHC-NC$_x$ (BFHC-NC$_0$, BFHC-NC$_5$, BFHC-NC$_{10}$) is revealed by the appearance of cathodic and anodic peaks in the potential range of 0~0.2 V from the CV curves. [57,58] However, noticeable variation in the CV curves including the redox peak position is observed on varying the carbon dioxide gas flow rate. For instance, BFHC-NC$_x$ prepared in nitrogen environment (BFHC-NC$_0$) display a weak redox peaks along with the appearance of quasi rectangular shapes at higher potential implying the capacitive type sodium-ion storage behaviour in this sample. On the contrary, two irreversible peaks is appeared in BFHC-NC$_x$ (BFHC-NC$_5$ and BFHC-NC$_{10}$) prepared in nitrogen and carbon dioxide environment. In the following cycles, irreversible reduction peak of the 1st cathodic peak disappear, which can be due to the decomposition of the electrolyte and creation of SEI film on the BFHC-NC$_x$ electrodes. This can be due to the lesser surface area/defect of the hard carbon electrodes and low heteroatoms content of the electrodes. A sharp reversible peak near at 0.02 V in the cathodic reduction could be due to Na-ions being inserted into the nano-crystalline graphitic planes, while the peak near at 0.2 to 0.15 in the anodic desodiation from the BFHC-NC$_x$ electrodes. In the subsequent cycles, the second and fifth cycle curves are approximately same, suggesting a balanced Na-ion storage behavior in BFHC-NC$_5$ and BFHC-NC$_{10}$ electrodes.

3.2.3 Sodiation mechanism

The first discharge- charge profiles of the hard carbon materials (BFHC-NC$_0$, BFHC-NC$_5$ and BFHC-NC$_{10}$) and its coulombic efficiencies measured at 0.1C rate are shown in **Figure 5.** Notable rise in charge/discharge capacities without significant variation in coulombic efficiency is observed in BFHC-NC$_5$ electrode in comparison to BFHC-NC$_0$ and BFHC-NC$_{10}$, revealing the enhanced sodium-ion (Na-ion) storage performance. As depicted in **Figure 5**, sodium-ion storage processes in the prepared BFHC are classified into three

different zones (i) adsorption zone (2.5V-0.25V) (ii) insertion zone (0.25V-0.02V) (iii) deposition zone(0.02V-0V) (**Figure S5).**[55,59,60]Appearance of the steep sloping potential above 2.5V-0.25V vs. Na^+/Na in all the hard carbon materials, corroborating the adsorption/chemisorption of Na-ions in the broken crystal edges, functional and defective sites of the BFHC-NCx. Relatively, steeper sloping potential ~ 0.15 V vs. Na/Na^+, a measure of sodium-ion adsorption/chemisorption process in BFHC-NC_5 sample, signifies its least contribution in Na-ion storage mechanism in comparison to the BFHC-NC_0 and BFHC-NC_{10} samples. Alternatively, significant rise in the plateau (insertion) zone on using N_2/CO_2 mixtures (BFHC-NC_5 and BFHC-NC_{10}), reveals the drastic improvement in the sodium-ion intercalation process in these systems, when compared to the samples prepared under nitrogen environment (BFHC-NC_0). About 75 % (BFHC-NC_5) and 70 % (BFHC-NC_{10}) increment in plateau (insertion) region is observed in the systems in comparison to the BFHC-NC_x prepared without CO_2 gas flow rate (BFHC-NC_0). No noticeable variation in electrode sodium-ion plating zone revealed constant sodium plating process in all the prepared BFHC-NC_x The voltage drop also termed as IR drop for the prepared BFHC-NC_x are observed to be 0.0119 (BFHC-NC_0), 0.00187 (BFHC-NC_5) and 0.0036 (BFHC-NC_{10}), respectively. Significant decrease in IR drop, a measure of ohmic resistance in the BFHC-NC_x anodes (BFHC-NC_5 & BFHC-NC_{10}), when compared to the BFHC-NC_0 may be correlated to the decrease in the kinetic sluggishness of sodium-ion (Na-ion) diffusion. Notable variation in disordered/ordered carbon phases of the BFHC-NC_x in the mixed gas environments (N_2/CO_2) is responsible for the variation in the adsorption/chemisorption, intercalation and plating of sodium-ions in the prepared BFHC-NC_x. Relative decrement in the insertion plateau zone (~70 %) at the higher CO_2 flow rate (10 ml min^{-1} of CO_2 gas flow rate; BFHC-NC_{10}), when compared to BFHC-NC_5 is attributed to the rise in disordered carbon/defective phases owing to the rise in pore size distribution.

3.2.4 Galvanostatic charge-discharge

The galvanostatic charge-discharge profiles of the prepared Borassus flabellifer male inflorescences (BFMI) derived hard carbon materials (BFHC-NC$_x$) electrode at a current rate of 0.1C between 0.01 and 2.5 V vs Na$^+$/Na are shown in **Figure 6(a,b)**. At the first charge/discharge profile, BFHC-NC$_5$ exhibits highest discharge/charge specific capacities of 413/358 mAhg^{-1} with a high initial discharge capacity retention of ~86.6%. Alternatively, discharge/charge specific capacities of BFHC-NC$_{10}$ are observed to be 405/338 mAh g^{-1} giving an initial discharge capacity retention of 83.4%. The above values are expressively higher, when compared to BFHC-NC$_0$ that display discharge/charge specific capacities of 375/272 mAh g^{-1} with initial discharge capacity retention of 76.4% (**Figure 6(a)**). The second galvanostatic discharge/charge profiles of the BFHC-NC$_x$ electrode measured at the current density of 20 mAg^{-1} further supports the above fact (**Figure 6(b)**). Furthermore, the second plateau discharge / charge capacity below 0.01 V is 367/356 mAhg^{-1}, 349/338 mAhg^{-1}, and 290/272 mAhg^{-1}, accounting for 97%, 96.8%, and 93.7% of the total reversible capacity for BFHC-NC$_5$, BFHC-NC$_{10}$, and BFHC-NC$_0$ respectively. Since the plateau capacity relates to Na-ion intercalation/de-intercalation from the hard carbon, the fallouts may propose improved Na-ion transport between carbon layers with relatively high defect attention. The BFHC-NC$_X$ electrode has the second cycle reach maximum initial columbic efficiency BFHC-NC$_5$ (98.8 %) relative to other BFHC-NC$_x$ electrodes *viz*., BFHC-NC$_{10}$ (96.5 %) and BFHC-NC$_0$ (92.4 %), respectively indicating that the irreversible responses mainly arise in the initial cycle and form stable SEI film. All the prepared hard carbon (BFHC-NC$_x$) electrodes provide the outstanding cycling stability after 10th cycles. These results can be correlated to the enhanced hard carbon nature, higher defect, and rough surface with enhanced broken edges, randomly distributed pore walls structures and variation in the

interlayer spacing's, aiding in the formation of a stable SEI layer on the surface of the BFHC-NC$_x$ electrodes.

3.2.5 Galvanostatic intermittent titration (GITT)

GITT test was done to further investigate the sodium ion diffusion coefficient and storage mechanism of BFHC-NC$_x$ electrodes are shown in **Figure 7(a-c)**. To understand the implications of gas flow rates on the electrochemical behaviors of BFHC-NC$_x$. in particular the defective hard carbon relationship with rate capability and sodium storage mechanisms. GITT was performed to represent the apparent Na$^+$ diffusion coefficient in BFHC-NC$_x$ electrodes with a pulse current of 10 mAg^{-1} for 1 hr during four-hour rest spacing. The sodium-ion diffusivity coefficient (D$_{Na+}$) can be calculated by the following generalized formula, based on Fick's second law (Eq-4):

$$D_{Na+} = \frac{4}{\pi\tau} \left(\frac{m_B V_M}{M_B S}\right)^2 \left(\frac{\Delta E_s}{\Delta E_\tau}\right)^2 \qquad (4)$$

Where τ is the pulse duration ($\tau << L^2/D_{K+}$), m$_B$ is the active mass of carbon materials, M$_B$ is the molar mass of carbon, V$_M$ is the molar volume of active materials and S is the surface area of the electrodes. The parameters ΔES and $\Delta E\tau$ are derived from the GITT results curves. The evident diffusivity coefficients of BFHC-NC$_x$ electrodes are in the range of 10^{-11} cm^2 s^{-1} and share a similar phenomenon in sodiation/desodiation process. In the process of sodiation, the diffusion coefficients first slightly descend, followed by a sudden drop to the lower part at 0.12 V and then recover before the limit voltage during the sodiation mechanism (**Figure 7(a-c)**). These notable variations can be correlated to the sodium-ion insertion mechanism in the graphitic microcrystals (in low potential platform range) and sodium-ion adsorption mechanism (in high potential slope range) (Zhu et al., J Mater. Chem.A, 2018). [61] From the GITT shows that the seeming diffusion coefficient with the inclination potential is substantially higher than the plateau. It is reasonable to assume that it is easier to reach the surface of turbostratic nanocrystallites than the layer region. As the surface active sites are

increasingly filled, sodium ions continue trying to diffuse into the turbostratic defective hard carbon. The GITT results show that different mechanisms describe the sodium processing system at sloping region and plateau zone. Sample BFHC-NC$_0$ and BFHC-NC$_{10}$ shows the lowest diffusivity of Na-ion at almost all specific potential,while BFHC-NC$_5$ displays the highest diffusivity of Na-ion. The strong sodium-ion diffusiveness can be due to the greater surface area of a large micro pore volume of 18.87 m^2 g^{-1}. Ultimately, the low potential for BFHC-NC$_5$ Na-ion storage can be attributed to its poor electronic conduction and a higher diffusiveness in Na-ion. Also one of the reasons fo the BFHC-NC$_5$ ability to be much greater than that of BFHC-NC$_0$ and BFHC-NC$_{10}$ at an established rate of 200 mA g^{-1} is improved Na-ion diffusivity. Therefore, the bigger size of graphitic nano domains in BFHC-NC$_5$ will result in a large plateau area capacity that cannot be shown at higher current rates. **Figure 7** shows that the sloping region diffusion coefficient is much higher than plateau region. Presenting those microspores, defective sites, and disordered carbon surface are occupied, Na$^+$ begins to implant in the more accessible than the graphite-like nanocrystals interlayer is rational.

The rate performance of prepared Borassus flabellifer male inflorescences (BFMI) derived hard carbon materials (BFHC-NC$_x$) electrode at a wide range of current rates from 20mA g^{-1} to 2000 mA g^{-1} (0.1 to 10 C), was used to evaluate the electrochemical kinetic properties of the prepared hard carbon materials (BFHC-NC$_x$), as shown in **Figure 8(a)**. The BFHC-NCx electrode present a less capacity fading when increase the current density. The prepared BFHC-NC$_5$ electrode as the best rate capability to other prepared electrodes and the average specific discharge capacities of 367, 328, 284, 248, 209, 151 and 117 mAh g^{-1} at the current density of 20, 40, 100, 200, 400, 1000 and 2000 mA g^{-1}, respectively. Similarly, BFHC-NC$_x$ electrode of the BFHC-NC$_{10}$ are 349, 289, 257, 219, 185, 134, and 81 mAh g^{-1} at the current density of 20,40, 100, 200, 400, 1000 and 2000 mA g^{-1}, respectively, and BFHC-

NC$_0$ are 290, 215, 174, 145, 109, 81, and 49 mAh g^{-1} at the current density of 20,40, 100,200,400,1000 and 2000 mA g^{-1} respectively. The long term electrochemical cycling behaviour of the BFHC-NC$_x$ electrodes is included in **Figure 8(b)**. The reversible average discharge capacities after 500 cycles are noted at a current rate of 20 mA g^{-1} with NaClO$_4$/EC: DEC electrolyte to be 332 mAh g^{-1} (BFHC-NC$_5$), 277 mAh g^{-1} (BFHC-NC$_{10}$) and 226 mAh g^{-1} (BFHC-NC$_0$), respectively. Higher discharge capacity with capacity retention of about 86.4% (BFHC-NC$_5$) and average columbic efficiency of >99.9% even after 500 cycles at 20 mA g^{-1}, revealed the enhanced electrochemical characteristics of BFHC-NC$_5$ samples and these results are in consistent with the CV results. From the galvanostatic charge-discharge profile, BFHC-NC$_5$ electrode presents the highest reversible capacity and efficiency, which can be credited to the improved interlayer spacing (0.360 nm), the comparative BET & PSD results and surface of the highly rough surface with wrinkles, enhanced broken edges and randomly distributed pore walls structures of the hard carbon electrode.

To elucidate the enhanced electrochemical properties and sodium ion storage mechanism, structural characterization of the BFHCM's-NC$_x$ extracted from the cycled electrode (0.1 C rate, 2nd & 500th cycles) was done using XRD and the results are included in **Figure S6 and Table S2.** And the morphological features of the cycled electrodes (2nd and 500th cycle) are shown in **Figure S7 and S8**. Finally, the comparation of Na-ion storage performance of biomass derived hard carbon materials available in the literature are tabulated (**Table S3).** [62-77]

3.2.6 EIS data interpretation for hard carbon

To further elucidate the interfacial chemistry and storage mechanism of prepared hard carbon (BFHC-NC$_x$) electrodes, electrochemical impedance measurements were done in the 100 kHz-0.01 Hz frequency range. The measured AC impedance in the form of typical Nyquist plots before and after cycling of BFHC-NC$_x$ electrodes are as shown in **Figure 8(c)**. Commonly, the impedance spectrum comprises of a depressed arc which is followed by an inclined straight

line (~45°). Various parameters such as internal ohmic resistance R_e (an intercept of the real axis (Z_{re}) plots at a high frequency region); resistance R_f and capacitance C_{dl1} at solid electrolyte interface (SEI); charge transfer resistance R_{ct} and capacitance C_{dl2} (in relevance to the semicircle region at a medium-to-low frequency region); Warburg impedance Z_w (parameter determined from the low frequency sloping region) were calculated using the equivalent circuit model and the values are listed in **Table 3**. The R_{ct} values decreased significantly after the 500th electrochemical cycling for all BFHC-NC$_x$ representing the corresponding rise in the electrical conductivity of the electrodes. Owing to its outstanding crystalline features, progressive decrement in the R_{ct} values with increasing pyrolytic temperature is observed corroborating lower charge-transfer resistance, thanks to its enhanced electrical conductivity. This fact is further strengthened by the R_{total} values taken before and after cycling which confirmed the faster electrode kinetics of the prepared BFHC-NC$_x$. Using the charge transfer resistance values, the exchange current density (i_0) was calculated and the results are included in **Table 3**. Progressive increment in exchange current density, i_0, with increasing pyrolytic temperature, implies enhanced electrochemical activity in these systems. Interestingly, the exchange current density (i_0) increases significantly for all BFHC-NC$_x$ revealing a noteworthy rise in the electrochemical activity after the 500th cycle.

Conclusion

An efficient method in preparing hard carbon materials (HCM's) from biomass Borassus flabellifer male inflorescences (BFMI) *via* a simple, single-step pyrolysis process has been reported for first time. Prepared defective hard carbon (BFHC-NC$_x$) offers a great potential in fulfilling the needs *viz.,* excellent electrochemical performance and sustainability of the sodium-ion battery electrodes, thus providing an opportunity for the forthcoming replacement to the current state-of-art lithium-ion batteries (LIBs). Owing to the turbostratic nature of the BFMI derived hard carbon materials with varying degree of defective sites,

enhanced broken crystal edges and randomly distributed pore walls, sodium-ion battery electrodes made with these carbon materials benefitted with the formation of stable solid electrolyte interface (SEI) film and efficient access to the electrolyte ions leading to the boosted diffusion process. When incorporated as an anode material for Na-ion batteries, the BFMI derived hard carbon materials exhibited a drastic reversible capacity, outstanding rate and electrochemical cycling stability. As reported in the literatures, the sodium-ion storage processes in the present BFMI derived carbon electrodes also exhibit three different storage mechanisms including adsorption, insertion and plating. However, depending on the experimental conditions used for the synthesis of biomass derived carbon, significant variation in the sodium-ion storage mechanism is observed. To revel, the prepared defective hard carbon (N_2:CO_2; 100:5 ml min^{-1} gas flow ratio with 1400°C) derived from Borassus flabellifer male inflorescences was found to display a highly rough surface with wrinkles, enhanced broken edges, randomly distributed pore walls structures etc. that aided to form a stable SEI film and efficient access of electrolyte ions to the carbon surface with enhanced ion diffusion and electrochemical property for SIBs. Conclusively, BFHC-NC$_5$ showed a higher degree of sodium-ion insertion mechanism, thus signifying the role of defective sites developed in the biomass derived carbon on the sodium-ion storage mechanism.

Acknowledgements

Declaration of interests

The authors declare that they have no known competing financial interests or personal relationships that could have appeared to influence the work reported in this paper.

Notes

† Electronic supplementary information (ESI) available.

Extra data on XRD, XPS, Raman spectroscopy, Cycled electrode data interpretation for hard carbon and plausible sodium ion storage mechanism in biomass derived hard carbon materials.

Credit Author Statement

Raghu Subashchandrabose conceived the research idea, designed the work plan, provided research guidance in executing the work, helped in data interpretation of electrochemical results as well as manuscript preparation. Thileep Kumar Kumaresan carried out research work, did material characterizations, fabricated coin cells, compiled the data and wrote the manuscript. Shanmugharaj Andikkadu Masilamani interpreted the material characterization results and helped in manuscript preparation. Kalaivani Raman & Smagul Zh. Karazhanov, provided research support in executing the research work

References

[1]. P. Wang, L. Fan, L. Yan, Z. Shi, J. Alloys Compd. 775 (2019) 1028-1035. https://doi.org/10.1016/j.jallcom.2018.10.180

[2]. S.Y. Hong, Y. Kim, Y. Park, A. Choi, N.S. Choi, K.T. Lee, Energy Environ. Sci. 6 (2013) 2067-2081. https://doi.org/10.1039/C3EE40811F

[3]. Y. Li, Y. Yuan, Y. Bai, et al., Adv. Energy Mater. 8 (2018) 1702781. https://doi.org/10.1002/aenm.201702781

[4]. F. Wu, M. Zhang , Y. Bai, X. Wang, R. Dong, C. Wu, ACS Appl. Mater. Interfaces. 11 (2019) 12554-61. https://doi.org/10.1021/acsami.9b01419

[5]. S. A. Ahad, R. Pitchai, A. M. Beyene, S. H. Joo, et al., Chem Sus Chem. 11 (2018) 3402-3409. https://doi.org/10.1002/cssc.201801432.

[6]. K. T. Kumar, M. J. K. Reddy, G. S. Sundari, S. Raghu, et al., Journal of Power Sources. 450 (2020) 227618. https://doi.org/10.1016/j.jpowsour.2019.227618.

[7]. D.A. Stevens, J.R. Dahn, J. Electrochem. Soc. 148 (2001) A803-811. https://doi.org/10.1149/1.1379565

[8]. M.I. Jamesh, A.S. Prakash,, J. Power Sources. 378 (2018) 268-300. https://doi.org/10.1016/j.jpowsour.2017.12.053

[9]. Z. Wang, L. Qie, L. Yuan, W. Zhang, X. Hu, Y. Huang, Carbon. 55 (2013) 328-334. https://doi.org/10.1016/j.carbon.2012.12.072

[10]. M. Hu, L. Yang, K. Zhou, C. Zhou, Z.H. Huang, F. Kang, R. Lv, Carbon. 122 (2017) 680-686. https://doi.org/10.1016/j.carbon.2017.05.003

[11]. J. Ni, S. Fu, Y. Yuan, L. Ma, Y. Jiang, L. Li, J. Lu, Adv. Mater. 30 (2018) 1704337. https://doi.org/10.1002/adma.201704337

[12]. X. Li, J. Ni, S.V. Savilov, L. Li, Chem. Eur. J. 24 (2018) 13719-27. https://doi.org/10.1002/chem.201801574

[13]. J. Ni, L. Li, J. Lu, ACS Energy Letters. 3 (2018) 1137-44. https://doi.org/10.1021/acsenergylett.8b00312

[14]. H. Kang, Y. Liu, K. Cao, et al., J. Mater. Chem. A. 3 (2015) 17899-913. https://doi.org/10.1039/C5TA03181H

[15]. X. Song, X. Li, Z. Bai, B. Yan, D. Li, X. Sun, Nano Energy. 26 (2016) 533-540. https://doi.org/10.1016/j.nanoen.2016.06.019

[16]. F. Tu, Y. Han, Y. Du, X. Ge, W. Weng, X. Zhou, J. Bao, ACS Appl. Mater. Interfaces. 11 (2018) 2112-9. https://doi.org/10.1021/acsami.8b19662

[17]. J. Liu, Y. Wen, P.A. van Aken, J. Maier, Y. Yu, Nano letters. 14 (2014) 6387-92. https://doi.org/10.1021/nl5028606

[18]. Y. Fang, X. Xu, Y. Du, X. Zhu, X. Zhou, J. Bao, J. Mater. Chem. A. 6 (2018) 11244-51. https://doi.org/10.1039/C8TA02945H

[19]. D. Goonetilleke, J.C. Pramudita, M. Choucair, A. Rawal, N. Sharma, J. Power Sources. 314 (2016) 102-108. https://doi.org/10.1016/j.jpowsour.2016.03.014

[20]. L. Wu, D. Buchholz, C. Vaalma, G.A. Giffin, S. Passerini, Chem Electro Chem. 3 (2016) 292-298. https://doi.org/10.1002/celc.201500437

[21]. E.M. Lotfabad, J. Ding, K. Cui, et al., ACS nano. 8 (2014) 7115-29. https://doi.org/10.1021/nn502045y

[22]. J. Xiang, W. Lv, C. Mu, J. Zhao, B. Wang, J. Alloys Compd. 701 (2017) 870-4. https://doi.org/10.1016/j.jallcom.2017.01.206

[23]. A.A. Arie, H. Kristianto, E. Demir, R.D. Cakan, Materials Chemistry and Physics. 217 (2018) 254-61. https://doi.org/10.1016/j.matchemphys.2018.06.076

[24]. D. Qin, Z. Liu, Y. Zhao, G. Xu, F. Zhang, X. Zhang, Carbon. 130 (2018) 664-71. https://doi.org/10.1016/j.carbon.2018.01.007

[25]. Q. Wang, X. Zhu, Y. Liu, Y. Fang, X. Zhou, J. Bao, Carbon. 127 (2018) 658-66. https://doi.org/10.1016/j.carbon.2017.11.054

[26]. C. Yu, H. Hou, X. Liu, Y. Yao, Q. Liao, Z. Dai, D. Li, Int. J. Hydrog. Energy. 43 (2018) 3253-60. https://doi.org/10.1016/j.ijhydene.2017.12.151

[27]. T. Zhang, J. Mao, X. Liu, et al., RSC advances. 7 (2017) 41504-11. https://doi.org/10.1039/C7RA07231G

[28]. N. Zhang, Q. Liu, W. Chen, et al., J. Power Sources. 378 (2018) 331-7. https://doi.org/10.1016/j.jpowsour.2017.12.054

[29]. L. Cao, W. Hui, Z. Xu, J. Huang, P. Zheng, J. Li, Q. Sun, J. Alloys Compd. 695 (2017) 632-637. https://doi.org/10.1016/j.jallcom.2016.11.135

[30].   Y. Zheng, Y. Wang, Y. Lu, Y.S. Hu, J. Li, Nano energy. 39 (2017) 489-498. https://doi.org/10.1016/j.nanoen.2017.07.018

[31].   Q. Li, Y. Zhu, P. Zhao, C. Yuan, M. Chen, C. Wang, Carbon.129 (2018) 85-94. https://doi.org/10.1016/j.carbon.2017.12.008

[32].   C. Bommier, W. Luo, W.Y. Gao, A. Greaney, S. Ma, X. Ji. Carbon. 76 (2014) 165-74. https://doi.org/10.1016/j.carbon.2014.04.064

[33].   J. Song, L. Wang, Y. Lu, et al., J. Am. Chem. Soc. 137 (2015) 2658-64. https://doi.org/10.1021/ja512383b

[34].   D. Saurel, B. Orayech, B. Xiao, D. Carriazo, X. Li, T. Rojo, Adv. Energy Mater. 1703268 (2018)1–33. https://doi.org/10.1002/aenm.201703268

[35].   H. Hou, X. Qiu, W. Wei, Y. Zhang, X. Ji, Adv. Energy Mater. 7 (2017) 1–30. https://doi.org/10.1002/aenm.201602898

[36].   J. Wang, P. Nie, et al., J. Mater. Chem. A. 5 (2017) 2411–2428. https://doi.org/10.1039/C6TA08742F

[37].   Z. Gao, Y. Zhang, N. Song, X. Li. Mater. Res. Lett. 5 (2017) 69–88. https://doi.org/10.1080/21663831.2016.1250834

[38].   Z. Li, C. Bommier, et al., Adv. Energy Mater. 7 (2017) 1602894. https://doi.org/10.1002/aenm.201602894

[39].   Y. Li, Y.S. Hu, M.M. Titirici, L. Chen, X. Huang, Adv. Energy Mater. 6 (2016) 1600659. https://doi.org/10.1002/aenm.201600659

[40].   Z. Li, Y. Chen, et al., Chemistry of Materials. 30 (2018) 4536-4542. https://doi.org/10.1021/acs.chemmater.8b00645

[41].   R. Väli, A. Jänes, T. Thomberg, E. Lust, J. Electrochem. Soc. 163 (2016) A1619-26. https://doi.org/10.1149/2.0771608jes

[42].   M. Sivachidambaram, J.J. Vijaya, et al., New J. Chem. 41 (2017) 3939-3949.

https://doi.org/10.1039/C6NJ03867K

[43]. T.K. Kumaresan, S.S. Gunasekaran, S.K. Elumalai, et al., Int. J. Hydrog. Energy. 44 (2019) 25918-25929. https://doi.org/10.1016/j.ijhydene.2019.08.044.

[44]. C.N. Barnakov, G.P. Khokhlova, A.N. Popova, S.A. Sozinov, Z.R. Ismagilov, Eurasian Chemico-Technological Journal. 17 (2015) 87-93. https://doi.org/10.18321/ectj198

[45]. F. Raj, R.M. Sundar, et al., Mater. Chem. Phys. 240 (2020) 122151. https://doi.org/10.1016/j.matchemphys.2019.122151

[46]. M. Yoshikawa, F. Xu, et al., Chem. Pharm. Bull. 55 (2007) 308-16. https://doi.org/10.1248/cpb.55.308

[47]. I. Izanzar, M. Dahbi, M. Kiso, S. Doubaji, S. Komaba, I. Saadoun, Carbon. 137 (2018) 165-73. https://doi.org/10.1016/j.carbon.2018.05.032

[48]. Cao, B., Liu, H., Xu, B., Lei, Y., Chen, X., & Song, H, J. Mater. Chem. A. 4 (2016) 6472-6478. https://doi.org/10.1039/C6TA00950F

[49]. V. Paillard, EPL. 54 (2001) 194. https://doi.org/10.1209/epl/i2001-00105-4

[50]. N. Shimodaira, A. Masui, Journal of Applied Physics. 92 (2002) 902-9. https://doi.org/10.1063/1.1487434

[51]. A.C. Ferrari, J. Robertson, Physical review B. 61 (2000) 14095. https://doi.org/10.1103/PhysRevB.61.14095

[52]. S. Hu, Y.L. Hsieh, RSC advances. 7 (2017) 30459-68. https://doi.org/10.1039/C7RA00103G

[53]. R. Kar, N.N. Patel, et al., Carbon. 106 (2016) 233-42. https://doi.org/10.1016/j.carbon.2016.05.027

[54]. A. Karatrantos, Q. Cai, Phys. Chem. Chem. Phys. 18 (2016) 30761-9. https://doi.org/10.1039/C6CP04611H

[55]. D. Er, J. Li, M. Naguib, Y. Gogotsi, V.B. Shenoy, ACS Appl. Mater. Interfaces. 6 (2014) 11173–11179. https://doi.org/10.1021/acsami.9b04774

[56]. M.K. Aydinol, A.F. Kohan, G. Ceder, J. Power Sources. 68 (1997) 664–668. https://doi.org/10.1016/S0378-7753(96)02638-9

[57]. S. Qiu, L. Xiao, M.L. Sushko, et al., Adv. Energy Mater. 7 (2017) 1700403. https://doi.org/10.1002/aenm.201700403

[58]. K. Tang, L. Fu, R.J. White, et al., Adv. Energy Mater. 2 (2012) 873-7. https://doi.org/10.1002/aenm.201100691

[59]. Y.E. Kim, S.J. Yeom, J.E. Lee, S. Kang, et al., J Power Sources. 468 (2020) 228371. https://doi.org/10.1016/j.jpowsour.2020.228371

[60]. S. Komaba, W. Murata, T. Ishikawa, N. Yabuuchi, T. Ozeki, et al., Adv. Funct. Mater. 21 (2011) 3859. https://doi.org/10.1002/adfm.201100854

[61]. Z. Zhu, F. Liang, Z. Zhou, X. Zeng, D. Wang, et al., J. Mater. Chem. A. 6 (2018) 1513-1522. https://doi.org/10.1039/C7TA07951F

[62]. A.A. Arie, B. Tekin, E . Demir, R. D. Cakan, Mater Technol. 34 (2019) 515. https://doi.org/10.1080/10667857.2019.1586087

[63]. X. Li, X. Zeng, T. Ren, J. Zhao, J. Alloys Compd. 787 (2019) 229. https://doi.org/10.1016/j.jallcom.2019.02.077

[64]. P.C. Rath, J. Patra, H.T. Huang, D. Bresser, et al., Chem Sus Chem. 12 (2019) 2302. https://doi.org/10.1002/cssc.201900319

[65]. S.D. Xu, Y. Zhao, S. Liu, X. Ren, et al., J. Mater. Sci. 53 (2018) 12334. https://doi.org/10.1007/s10853-018-2472-4

[66]. S. Zhang, Y. Li, M. Li. JOM. 70 (2018) 1387. https://doi.org/10.1007/s11837-018-2789-0

[67]. J. Wang, L. Yan, Q.J. Ren, L.L. Fan, et al., Electrochim Acta. 291 (2018) 188. https://doi.org/10.1016/j.electacta.2018.08.136

[68]. Y.Y, Zhu, M.M. Chen, Q. Li, C. Yuan, et al., Carbon. 129 (2018) 695. https://doi.org/10.1016/j.carbon.2017.12.103

[69]. M. Dahbi, M. Kiso, K. Kubota, T. Horiba, et al., J. Mater. Chem. A. 5 (2017) 9917. https://doi.org/10.1039/C7TA01394A

[70]. Z. Zhu, F. Liang, Z. Zhou, X. Zeng, et al., J. Mater. Chem. A. 6 (2018) 1513. https://doi.org/10.1039/C7TA07951F

[71]. C. Wang, J. Huang, H. Qi, L. Cao, et al., J. Power Sources. 358 (2017) 85. https://doi.org/10.1016/j.jpowsour.2017.05.011

[72]. F. Shen, W. Luo, J. Dai, Y. Yao, et al., Adv. Energy Mater. 6 (2016) 1600377. https://doi.org/10.1002/aenm.201600377

[73]. P. Liu, Y.M. Li, Y.S. Hu, H. Li, et al., J. Mater. Chem. A. 4 (2016) 13046. https://doi.org/10.1039/C6TA04877C

[74]. H. Li, F. Shen, W. Luo, J. Dai, et al., ACS Appl. Mater. Interfaces. 8(2016) 2204. https://doi.org/10.1021/acsami.5b10875

[75]. F. Zhang, Y. Yao, J. Wan, D. Henderson, et al., ACS Appl. Mater. Interfaces. 9 (2017) 391. https://doi.org/10.1021/acsami.6b12542

[76]. N. Sun, H. Liu, B. Xu. J. Mater. Chem. 3 (2015) 20560. https://doi.org/10.1039/C5TA05118E

[77]. E.M. Lotfabad, J. Ding, K. Cui, A. Kohandehghan, et al., ACS Nano. 8 (2014) 7115. https://doi.org/10.1021/nn502045y
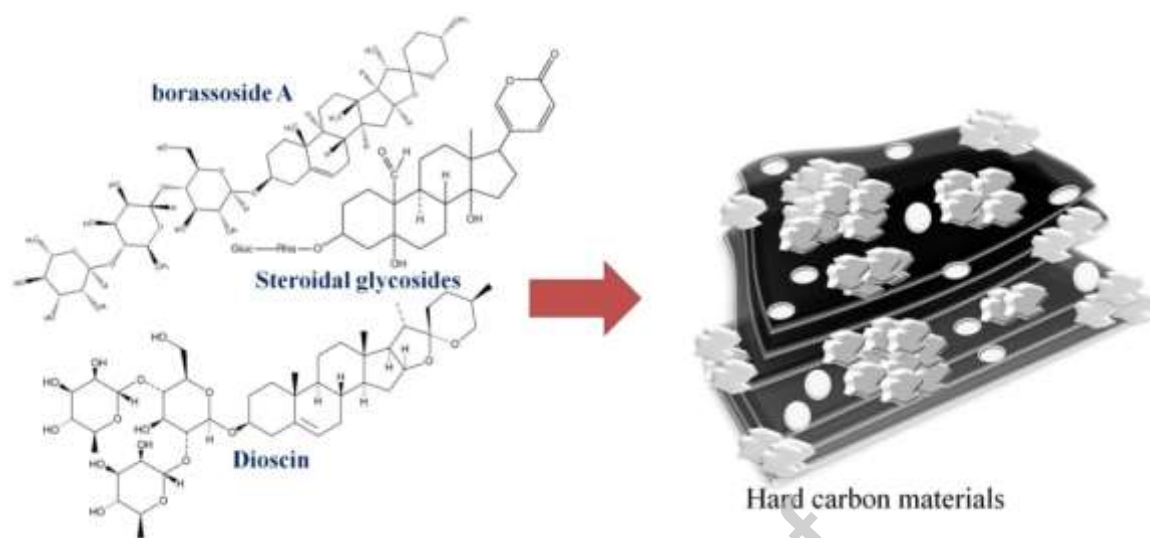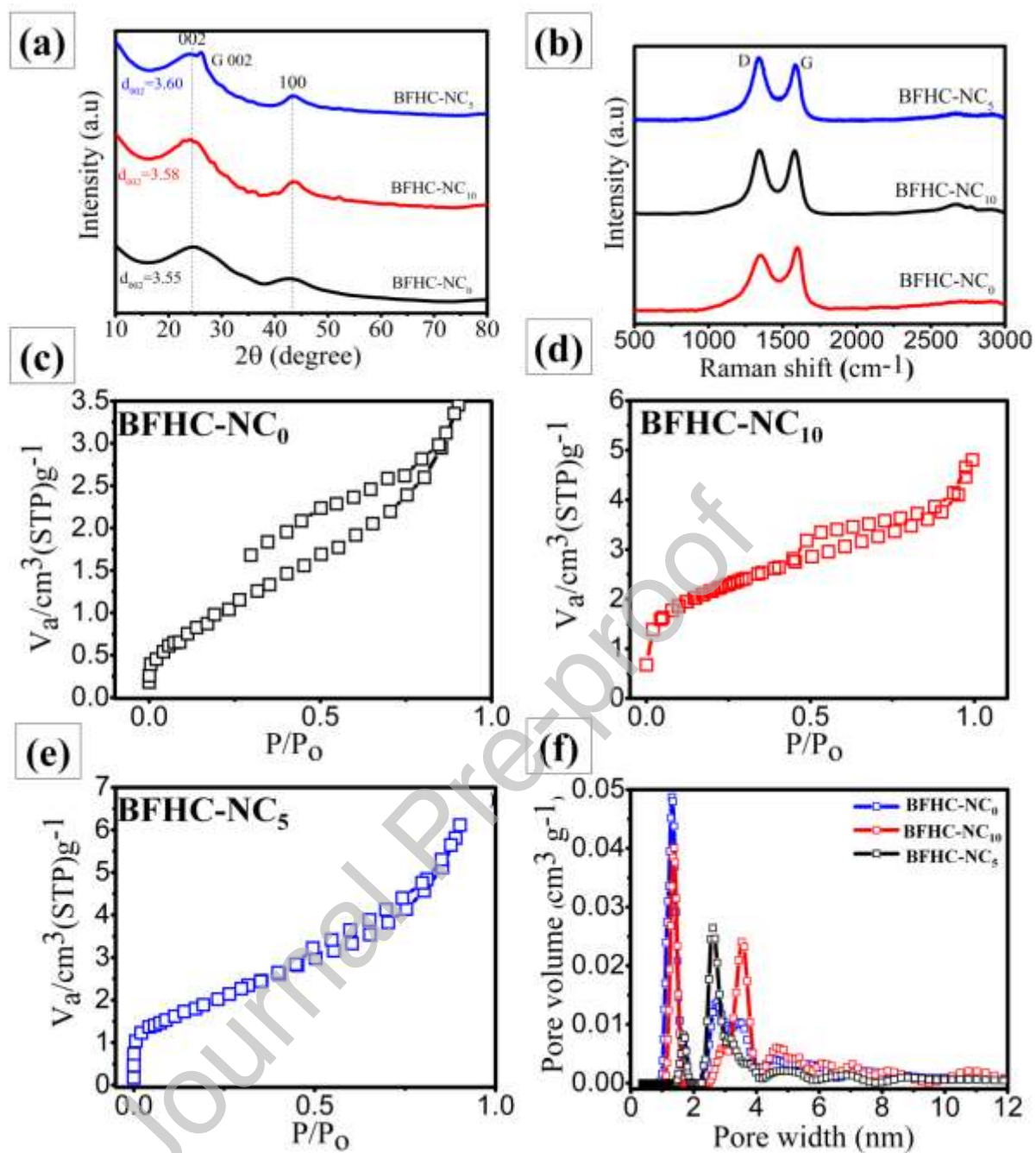
Figure 1 Schematic representation of BFMI (saponins, glycosides and carbohydrates) to the formation of highly disordered hard carbon materials.
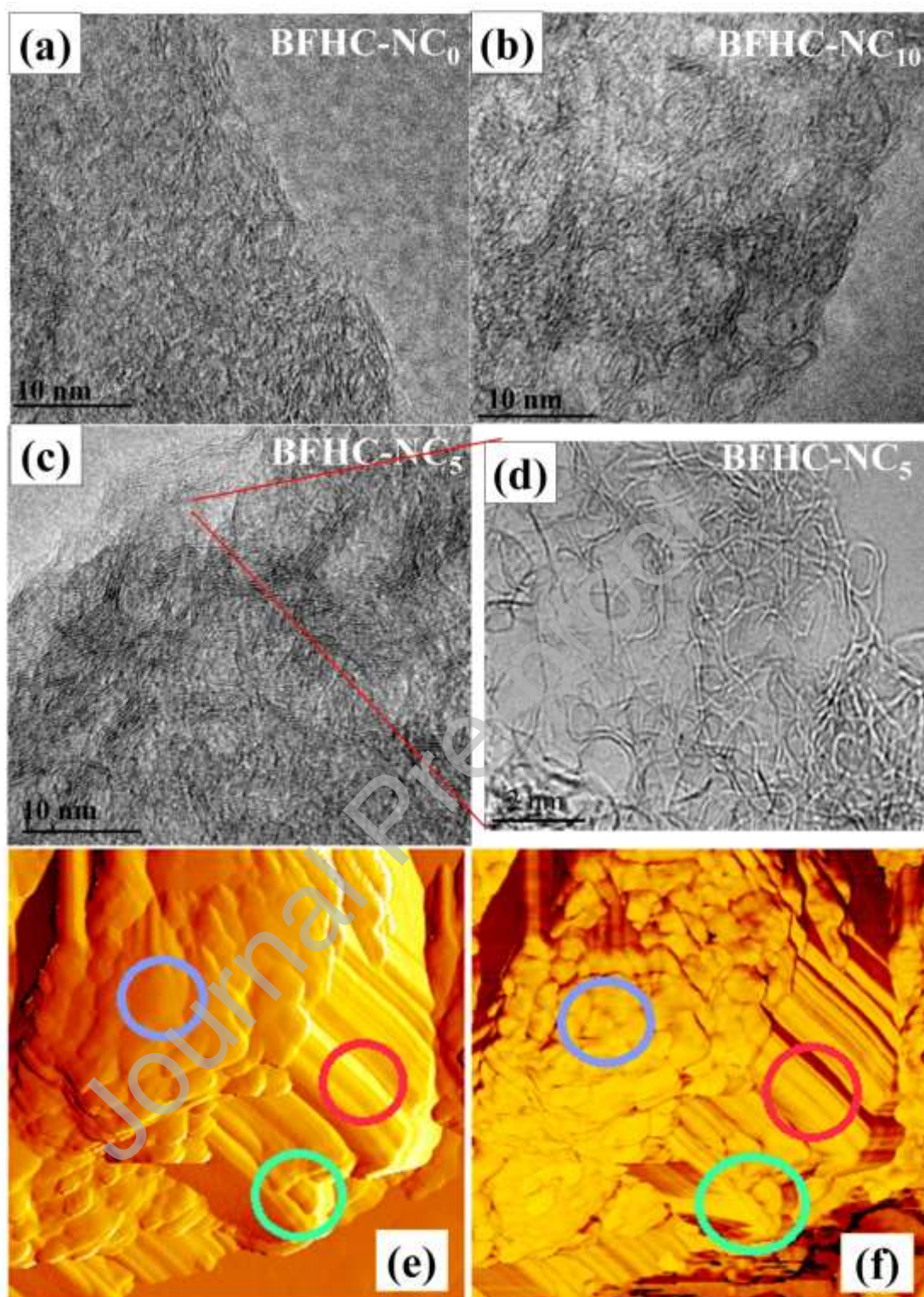
Figure 2. HRTEM images of (a) BFHC-NC$_0$ (50nm); b) BFHC-NC$_{10}$ (50nm); (c) BFHC-NC$_5$

(50nm) and (d) BFHC-NC$_5$ at higher Magnifications (~5nm); AFM images for the amplitude

(e) and phase (f) images of the BFHC-NC$_5$ sample.

Figure 3 (a) XRD pattern and (b) Raman spectra of hard carbon materials thermally treated

with different gas flow rate for BFHC-NC$_0$, BFHC-NC$_{10}$, BFHC-NC$_5$;

N$_2$ adsorption isotherms and related PSDs of the BFHC- NC$_x$ samples. (c) Nitrogen isotherms

of BFHC-NC$_0$; (d) Nitrogen isotherms of BFHC-NC$_{10}$; (e) Nitrogen isotherms of BFHC-NC$_5$;
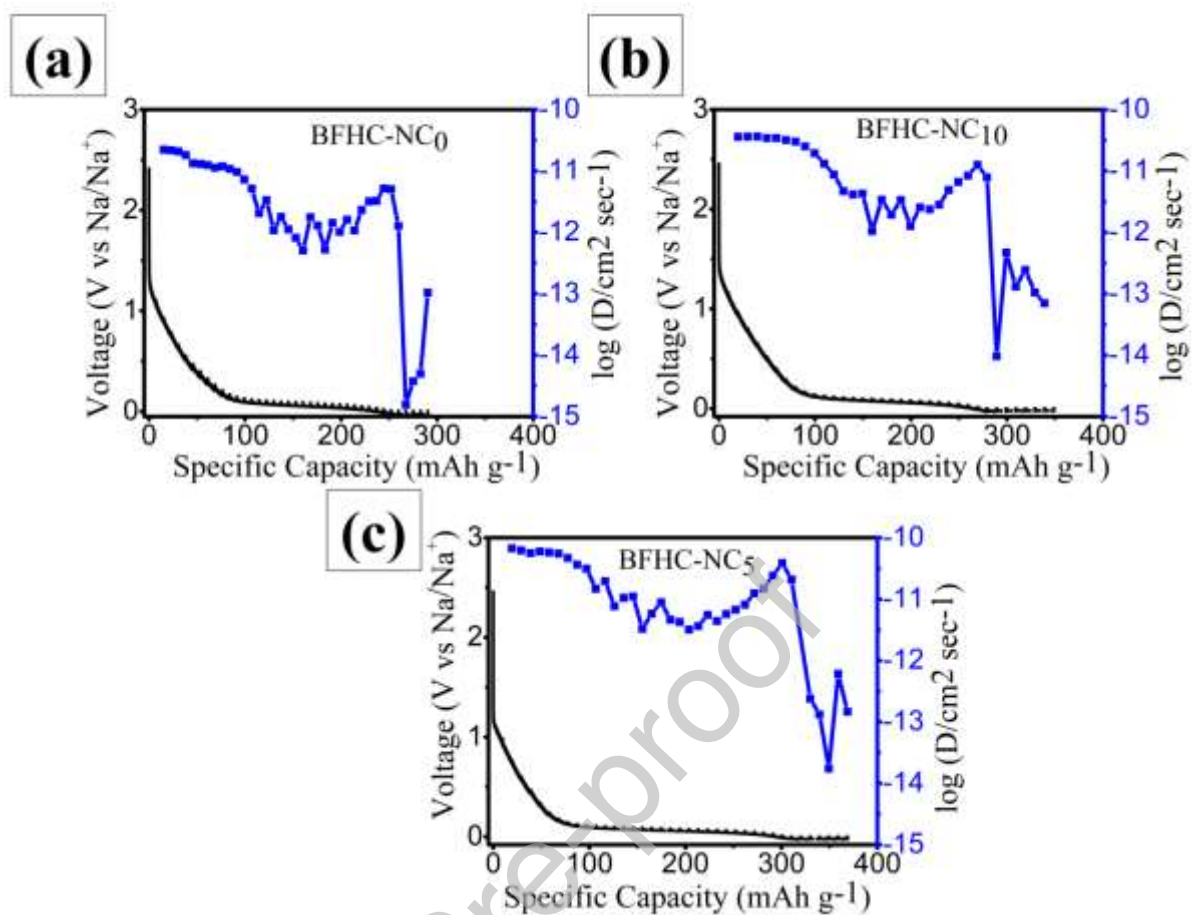
(f) PSDs of BFHC- NC$_x$.
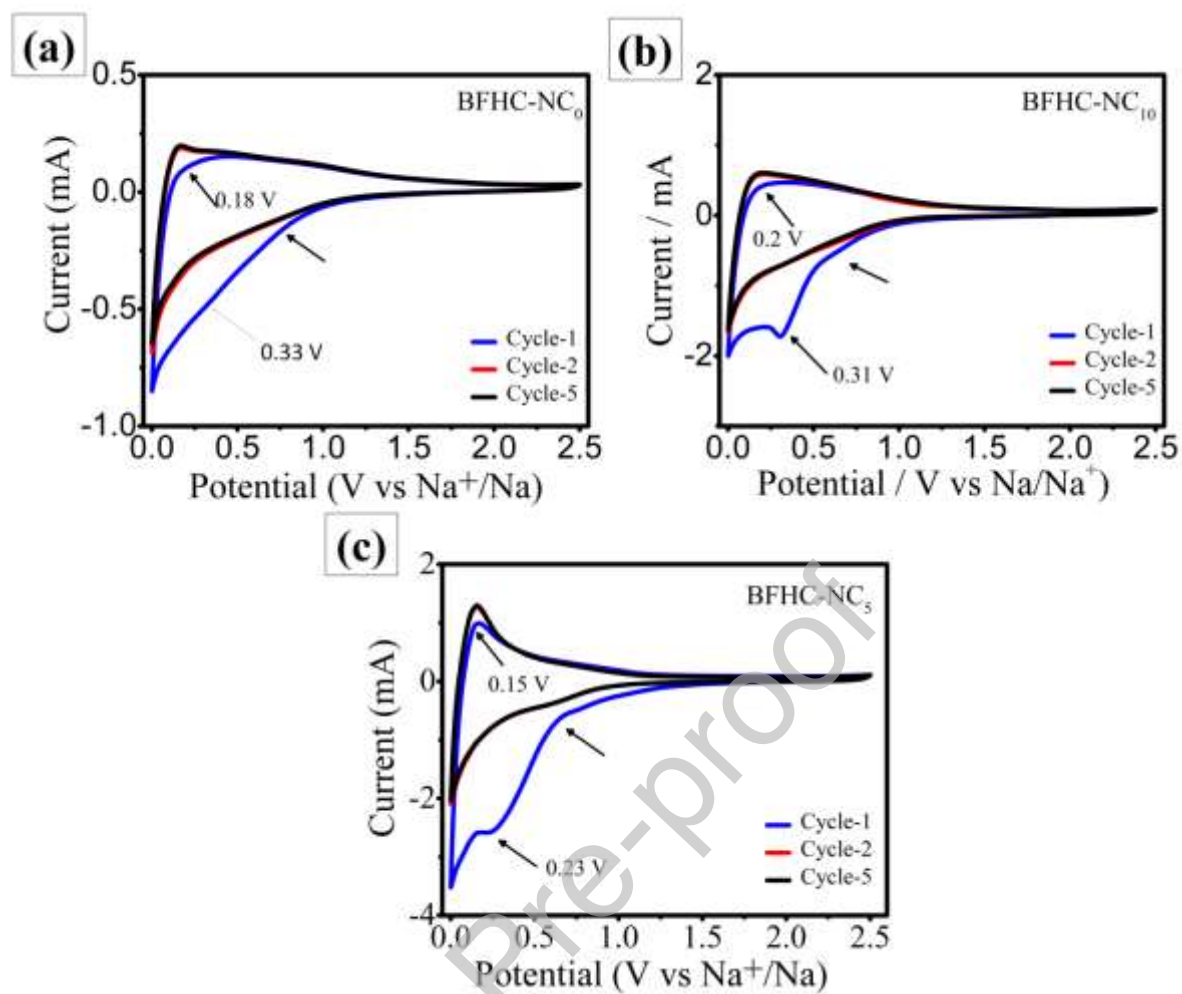
Figure 4 Cyclic voltammogram (CV) measured in the potential range of 0.001~2.5 V at the scanning speed of 0.5mVs^{-1} of the prepared hard carbon materials (a) BFHC- NC$_0$; (b) BFHC- NC$_{10}$;(c) BFHC- NC$_5$
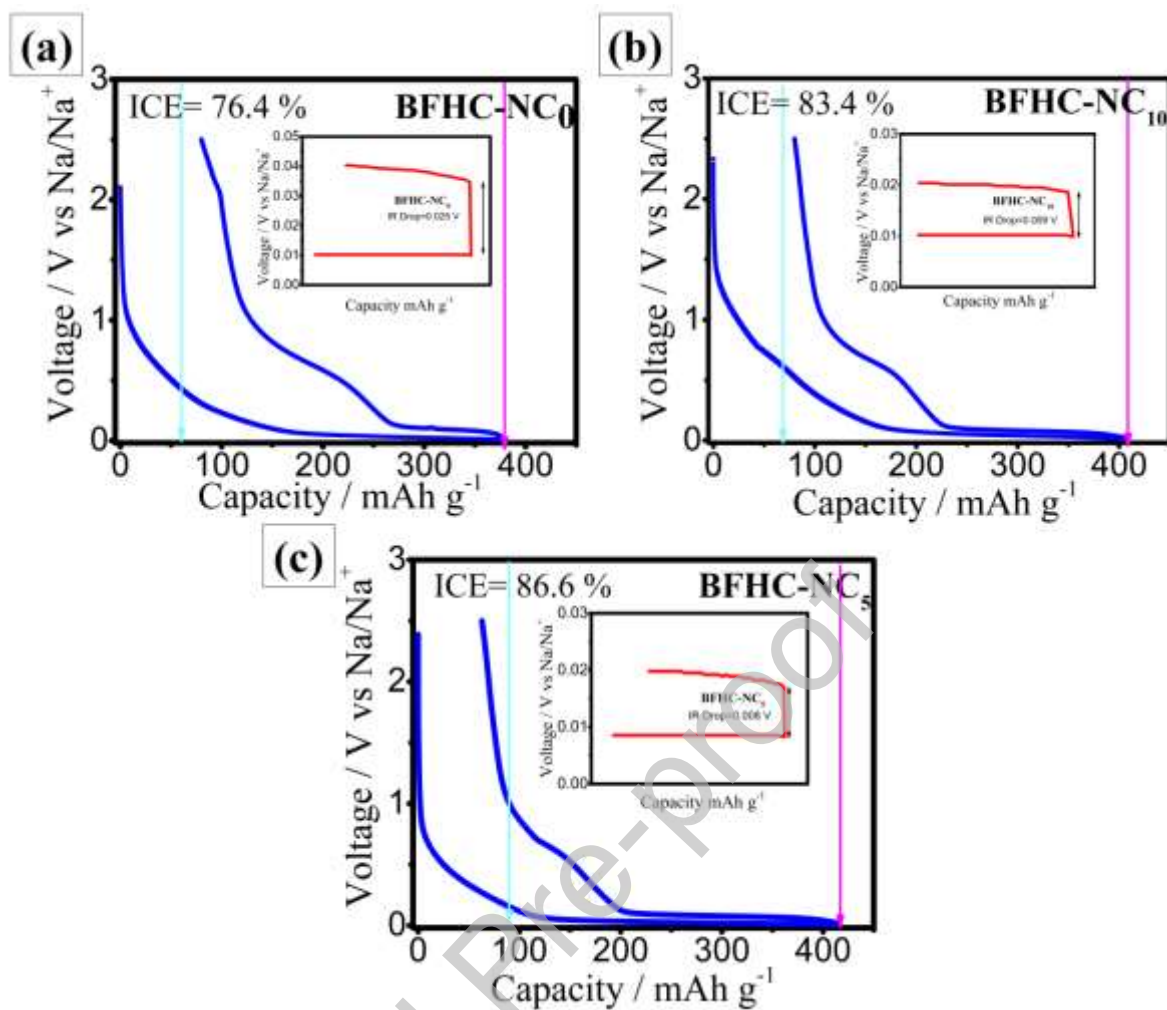
Figure 5 The first charge-discharge profiles with mechanisum of the prepared hard carbon materials ((a) BFHC-NC₀, (b) BFHC-NC₁₀, (c) BFHC-NC₅) measured at 0.1C rate, (Inside: IR drop)
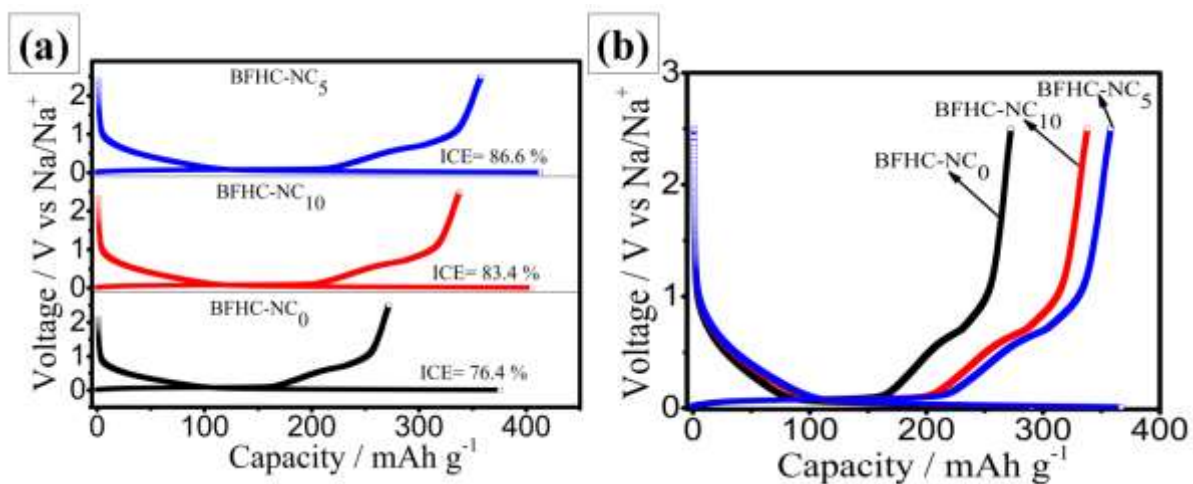
Figure 6 a) The galvanostatic charge-discharge profiles of the prepared hard carbon (BFHC- NC_x) electrodes at a current rate of 0.1C between 0.01 and 2.5 V vs Na/Na$^+$ (a) first cycle, (b) second cycle.

Figure 7 GITT potential profiles of BFHC –NC$_x$ electrodes for sodiation during the second cycle; Sodium ions apparent diffusion coefficients estimated from the GITT potential profiles of BFHC –NC$_x$ electrodes for sodiation during the second cycle.

t
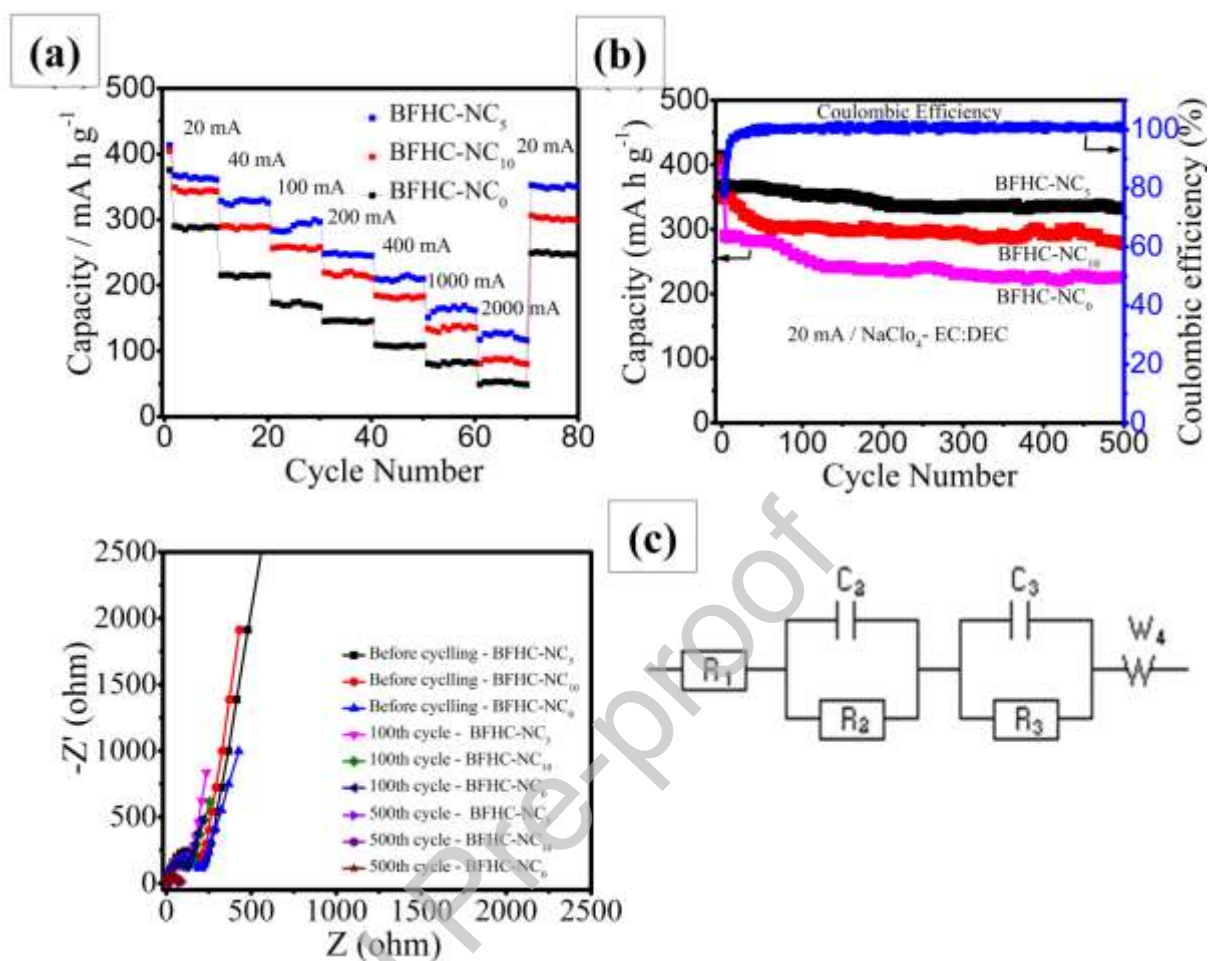
Figure 8 (a) Rate capability of BFHC- NC$_x$ electrodes from 20 mAh to 2000 mAh. (b) Cycle performances of BFHC- NC$_x$ electrodes at a current rate of 20 mAh at 500 cycles. (**c**) Electrochemical impedance spectroscopy (EIS) of measurements in the frequency range of 100 kHz-0.01 Hz. [circuit diagram, here R$_1$=R$_e$; R$_2$=R$_f$; R$_3$= R$_{ct}$; C$_2$= C$_{d11}$; C$_3$=C$_{d12}$;

Table 1 XRD peak and fitting of the d002 peak of the XRD pattern of the prepared hard carbons.

Samples	Phase	2Θ (002)							2Θ (100)
		Phase fraction	FWHM	d002 (Å)	Lc (Å)	g	N	p	La (Å)
BFHC-NC₀	Disordered region	56.3	5.48	3.70	14.8	-3.25	7.22	2.04	-
	Graphitic region	43.7	6.12	3.20	13.4	2.32	19.6	2.35	-
	Without phase separation	-	8.15	3.55	10.1	-1.28	2.84	2.15	35.3
BFHC-NC₅	Disordered region	48.2	4.76	3.85	17.1	-4.30	4.43	2.0	-
	Graphitic region	51.8	2.83	3.40	28.2	0.11	8.23	2.22	-
	Without phase separation	-	5.84	3.60	14.1	-1.86	3.91	2.12	52.1
BFHC-NC₁₀	Disordered region	51.8	5.36	3.82	15.1	-4.76	4.33	1.98	-
	Graphitic region	48.2	5.69	3.37	14.4	0.81	11.8	2.26	-
	Without phase separation	-	7.37	3.58	11.2	-1.62	3.11	2.13	48.4

*d002 – interlayer spacing was calculated by the Bragg equation with the center of the (002) diffraction peak, Lc – layer stacking distance, La – longitudinal dimension of a stack, ρ – layer packing density, N – Number of graphene layer , g -The degree of graphitization.

Table 2 Raman and BET characterisation results for hard carbon (BFH's- NC_x)

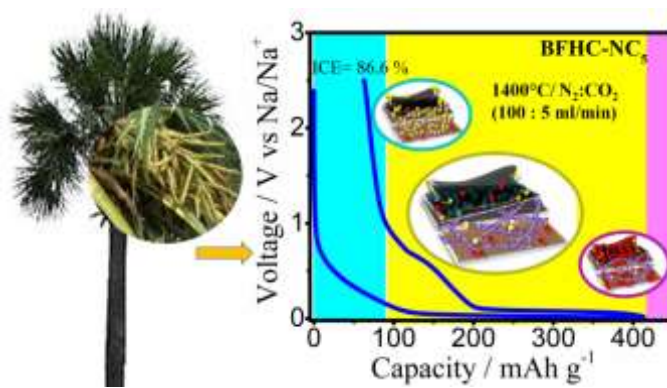| Hard carbon materials	I_D/I_G ratio De-Conversional data		(S_{BET}) $(m^2\,g^{-1})$	(V_P) $(cm^3\,g^{-1})$	(D_P) (nm)	(Vm) $(cm^3\,g^{-1})$
	I_{D1}/I_{G1}	I_{D2}/I_{G2}				
BFHC-NC$_0$	1.35	0.36	4.08	0.00534	5.236	0.937
BFHC-NC$_5$	0.77	0.86	18.87	0.00945	5.31	1.635
BFHC-NC$_{10}$	1.03	0.80	8.86	0.00752	5.28	1.245

S_{BET} - BET surface area, V_P - Pore volume, D_P -Mean pore diameter, V_m- Volume of adsorbed nitrogen on the carbon surface.

Table 3 EIS data interpretation for hard carbon (BFHC's- NC_x)

	Hard carbon materials		
	BFHC-NC$_0$ Before Cycle (Ohm)	**BFHC-NC$_5$** Before Cycle (Ohm)	**BFHC-NC$_{10}$** Before Cycle (Ohm)
R$_e$	6.423	9.419	8.74
R$_f$	36.95	46.7	42.9
R$_{ct}$	22.7×10^{-9}	14.11×10^{-9}	16.9×10^{-9}
Rtotal	96.2	85.4	88.5

[Here $R_1=R_e$; $R_2=R_f$; $R_3=R_{ct}$]

Graphical Abstract